Electronic Supplementary Information

Permeation properties and hydrothermal stability of Allylhydridopolycarbosilane (AHPCS)–derived Silicon Carbide (SiC) membranes

Gusni Sushanti,[a] Daiki Tanabe,[a] Khuat Thi Thu Hien,[a] Norihiro Moriyama,[a] Hiroki Nagasawa,[a] Masakoto Kanezashi,[a] Toshinori Tsuru*[a]

[1]Department of Chemical Engineering, Hiroshima University, 1-4-1 Kagami-yama, Higashi-Hiroshima

739-8527 Japan

Corresponding author:

Toshinori Tsuru, tsuru@hiroshima-u.ac.jp

Contents

AHPCS membrane performance at 200 °C before hydrothermal treatment (HT) at different firing temperatures.

The permeance of single gas through an AHPCS-derived membrane was measured at a temperature of 200 °C. Single gas permeance is useful for evaluating the pore size distribution of membranes and is the simplest method for determining membrane quality. Generally, all membranes showed decreased permeance for large-sized gases, indicating typical molecular sieving properties. The H_2/N_2 selectivity ranged from 10–20 with excellent H_2 permeance higher than 10^{-6} mol/(m^2 s Pa).
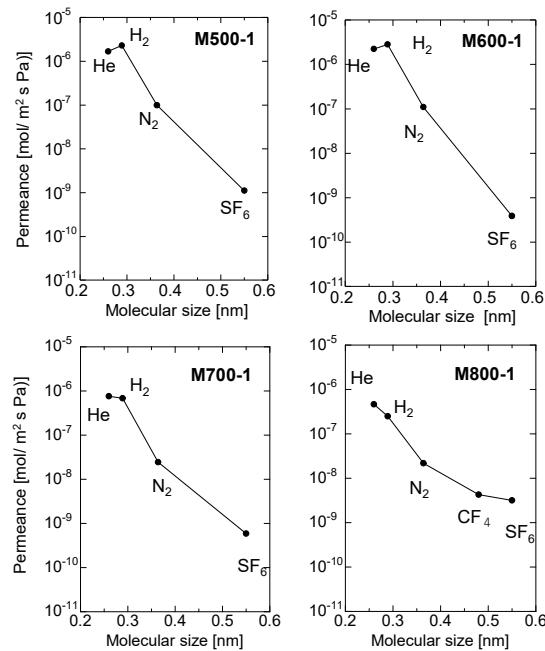
Fig. S1 Single gas permeance at 200 °C as a function of molecular size through AHPCS membranes formed at different firing temperatures.

Table S1. AHPCS membrane performance at 200 °C before hydrothermal treatment (HT) at different firing temperatures.

Membranes	Permeance (10^{-8} [mol /(m^2 s Pa)])			
	He	H_2	N_2	SF_6
M500-1	168	230	10	0.11
M600-1	223	282	11	0.04
M700-1	76	68.3	2.44	0.06
M800-1	46	24.9	2.18	0.32

Membranes	Seletivity [-]		
	He/H$_2$	H$_2$/N$_2$	H$_2$/SF$_6$
M500-1	0.73	23.23	2090.91
M600-1	0.79	25.66	7287.62
M700-1	1.11	27.98	1159.93
M800-1	1.86	11.43	78.61

Activation energy of H$_2$ for each membrane.

The temperature dependency (200–400 °C) of H$_2$ permeance was also evaluated on the AHPCS-derived membrane and used to obtain the activation energy of H$_2$. Notably, the activation energy was obtained by regressing the temperature dependence of the H$_2$ permeance for temperatures ranging from 200 to 400 °C using the translation model.[1]

$$Pi = \frac{k_{0,i}}{\sqrt{M_i RT}} exp\left(-\frac{E_{p,i}}{RT}\right),$$

where $k_{0,i}$ is the pre-exponential factor; $E_{p,i}$ is the permeation activation energy; M_i is the molecular weight of the ith component; R is the gas constant; and T is the absolute temperature.[2]

Membranes	Ep H$_2$ (kJ/mol)
M500-1	2.6
M500-2	3.6
M550-1	2.8
M550-2	2.1
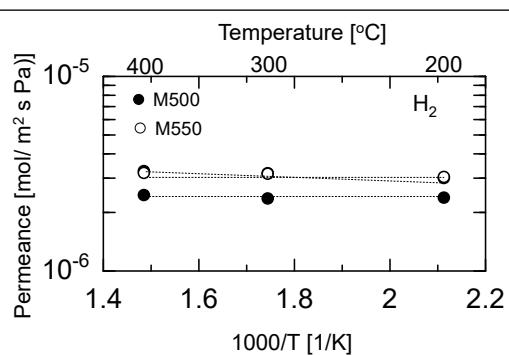
Membranes	Ep H$_2$ (kJ/mol)
M600-1	2.4
M600-2	3.6
M600-3	3.4

Membranes	Ep H$_2$ (kJ/mol)
M700-1	7.3
M700-2	6.3
M800-1	4.6
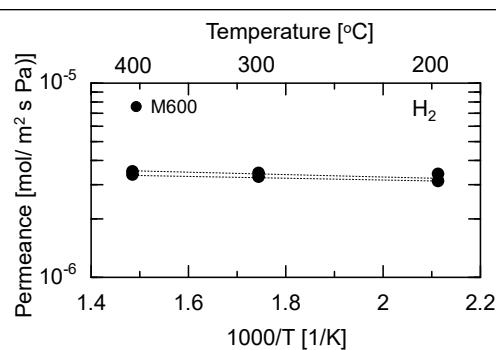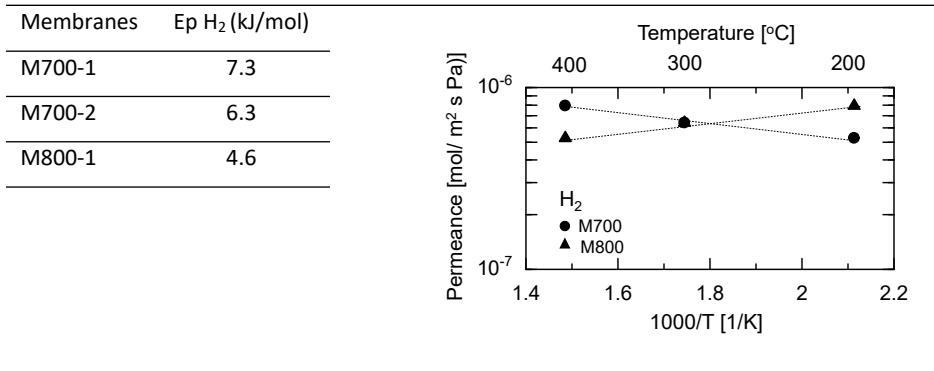
Fig. S2. Activation energy of H$_2$ for each membrane

FESEM image of cross section of low magnification (x50,000) (a), and of high magnification (x150,000) (b)

FESEM images illustrating the cross section of low and high magnification of the M700 membrane are presented in Figs. S3 (a) and (b), respectively. The estimated thickness of the top layer, including the intermediate layer, is approximately 200 nm (Fig. S3 (a)). Fig. S3(b) shows the SEM image of high magnification of the area surrounded by the dotted lines in Fig. S3(a), indicating top layer thickness is around 30 nm. This thin top layer has the potential to impart the resulting membrane with high gas permeability and molecular sieving properties.
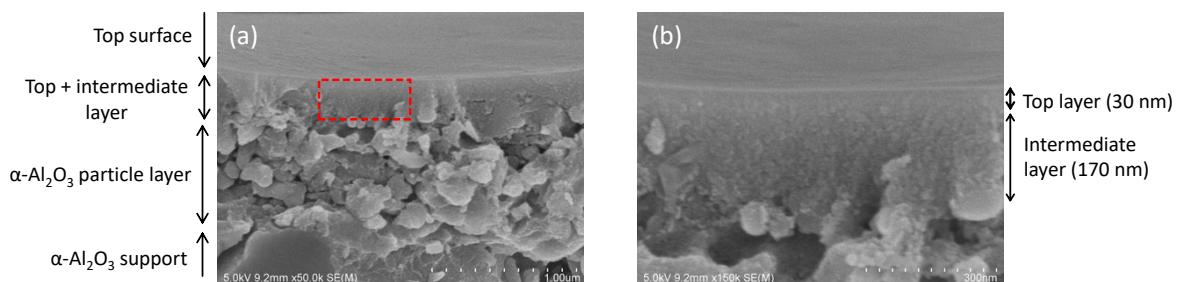
Fig. S3 FESEM image of cross section of low magnification (x50,000) (a), and of high magnification (x150,000) (b)

DTG curves of weight residue of AHPCS at different temperatures.

The process of turning AHPCS precursors into ceramics involves three main stages. First, polymer phase (T ≤ 400°C) consists mainly of connected polymer chains. Second, transition phase (400°C < T < 700°C) involves the decomposition of the organic groups. This phase is a transition for getting the materials ready for ceramic conversion. Third, in ceramic phase (T ≥ 700°C), the material enters the ceramic phase. We performed TGA (Thermogravimetric Analysis) measurements to assess thermal stability. The steps for TG measurements mirrored those of membrane fabrication. Initially, the sample underwent heating at 100°C for 1.5 hours to eliminate any water content present on the powder. Subsequently, the temperature was raised to various levels (500–800°C) at a rate of 5°C per minute and held at each temperature for 1 hour under N_2. As shown in the time course (Figs. S4 (a), (b), (c), (d)), the weight residue remained constant after reaching each temperature, confirming the thermal stability. Fig S4 (e) shows the summary of weight residue after holding 1 h at different temperatures. The material undergoes a gradual reduction in weight as the temperature increases, signifying a process of thermal decomposition and/or transformation from polymer ceramic phase, which induces the formation of a denser network within the material.
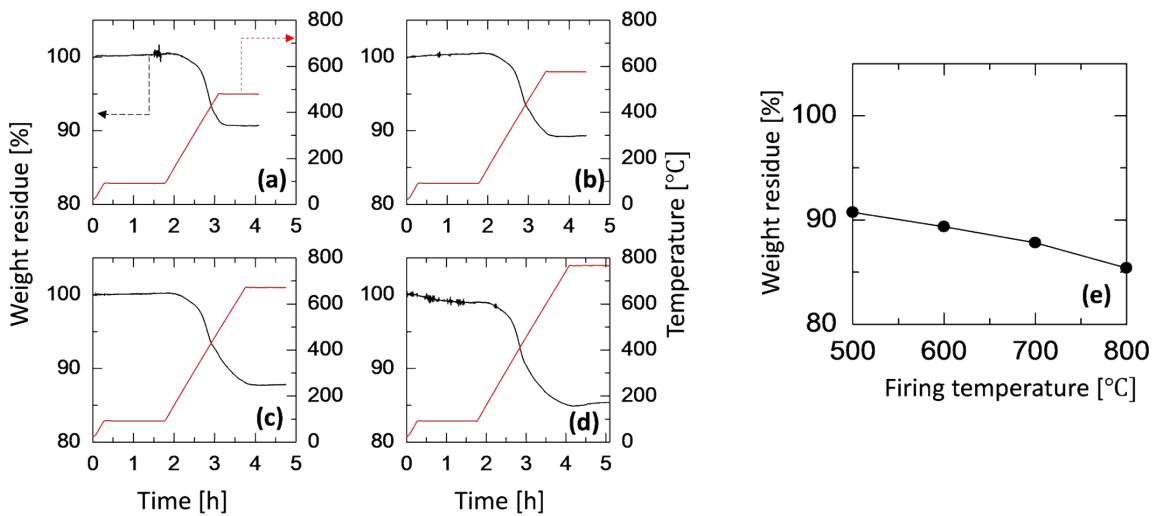

Fig. S4 Time course of thermal treatment (a) 500 °C, (b) 600 °C, (c) 700 °C, (d) 800 °C, and (e) weight residue of AHPCS at different temperature. (N_2 flow rate 50 ml/min, heating rate of 5 °C/min).

Schematic illustration of surface structure changed after hydrothermal treatment.

The steam oxidation of SiC at high temperatures (1400–1800 °C) can be categorized into two different processes, known as SiO_2 formation and its volatilization.[3] The formation of both a condensed SiO_2 oxide and volatile phases, such as $Si(OH)_4$, is induced at the same time. SiC reacts with water vapor to form SiO_2 on the SiC surface via the following reaction:

$$SiC_{(s)} + 3H_2O_{(g)} = SiO_2 + 3H_{2(g)} + CO_{(g)}. \qquad (1)$$
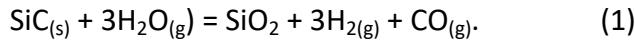
On the surface, the oxide scale reacts with water vapor at high temperatures and undergoes volatilization via, the following reaction:

$$SiO_{2(s)} + 2H_2O_{(g)} = Si(OH)_{4(g)}. \qquad (2)$$
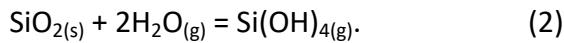
In the meantime, at the interface, SiC reacts to form SiO_2, with H_2O or oxidizing OH• or H• radicals.[4] This reaction (Eq. 1) also reportedly occurred at 600 °C although conversion to silica was low around 1%,[5] and it may have occurred at 400 °C.

SiC-based membranes are expected to be more hydrothermally stable than SiO_2 and organosilica membranes due to the incorporation of carbon elements in the silica structure. The decrease in N_2 permeance can be attributed to the formation of -OH (Si-OH) groups on the surface of the membrane pores. The pore size of the membrane decreases after HT due to water vapor oxidation. This reduction in pore size results in decreased permeation of larger gas molecules, such as N_2. Specifically, the molecular sizes follow the order N_2 > H_2O > He, with sizes of (kinetic diameter: 0.364^6 nm, 0.265^7 nm, 0.26^8 nm), respectively. The obtained results align with findings from experiments conducted using carbonized-template molecular sieve silica membranes under hydrothermal conditions (400°C, steam: 34 kPa).[9,10]

Upon exposure to high temperatures of steam, the AHPCS membrane undergoes a reaction with water vapor, forming Si-OH groups. Si-H groups oxidize (Eq. 3) to form Si-OH groups, which further undergo condensation to create Si-O-Si linkers (Eq. 4), resulting in a denser network structure. This densification leads to a reduction in pore size, limiting the movement of gas molecules through the membrane and subsequently lowering the gas permeation rate (Fig. S3). The observed changes are consistent with the triethoxysilane (TRIES) silica membrane network structure, where a decrease in Si-H groups correlates with a denser network under hydrothermal conditions.[11]

$$\equiv Si - H + H_2O \rightarrow \equiv Si - OH + H_2 \qquad (3)$$

$$2 \equiv Si - OH \rightarrow \equiv Si - O - Si\equiv + H_2O \qquad (4)$$

Formation of SiOH
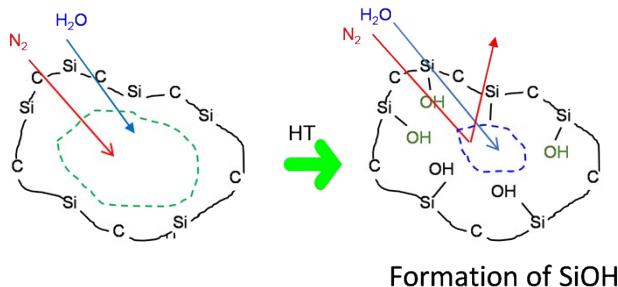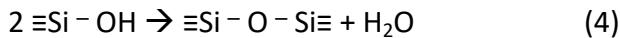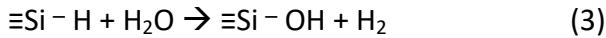
Fig. S5. Schematic illustration of surface structure changed after hydrothermal treatment.

Permeance and selectivity at 200 °C before and after hydrothermal treatment (HT) of membrane firing from 500–800 °C.

The gas permeance ratio determines the selectivity and is commonly employed as an index for evaluating membrane quality. The selectivity before feeding water vapor, indicated as "0HT," is a crucial parameter. Similarly, the selectivity after the 1st, 2nd and 3rd HT is denoted as "1HT," "2HT" and "3HT." After subjecting the membranes to HT, the selectivity of He/H_2 increased for M500 to M700, but decreased for M800. This was attributed to the denser membrane pores in M800, making it easier for He to permeate than H_2. In contrast, the H_2/N_2 selectivity reached its peak at M600 after HT, showing an almost four-fold increase compared with that before HT. However, the selectivity of H_2/SF_6 decreased for all membranes after HT, as pinholes were formed during the treatment, leading to reduced selectivity.

The permeance values of He, N_2, and SF_6, were measured before and after 3HT. After subjecting the membranes to three HT cycles, the permeance of all gases decreased, except for that of SF_6. The reduction in permeance can be attributed to the shrinkage of the membrane pores, whereas the increase in SF_6 permeance was attributed to the presence of pinholes.

Table S2. Comparison permeance and selectivity at 200 °C before and after hydrothermal treatment (HT) of membrane firing from 500–800 °C.

Membranes	Permeance (10^{-8} [mol /(m² s Pa)])															
	He				H_2				N_2				SF_6			
	0 HT	1 HT	2 HT	3 HT	0 HT	1 HT	2 HT	3 HT	0 HT	1 HT	2 HT	3 HT	0 HT	1 HT	2 HT	3 HT
M500-1	168	54	46.8	44	230	60	52.7	46	10	2.1	2.04	2	0.11	0.2	0.3	0.3
M600-1	223	75	52	40.5	282	51.2	30.1	20.9	11	0.6	0.4	0.28	0.04	0.03	0.03	0.1
M700-1	76	46.8	19.3	14.1	68.3	52.7	9.27	3.3	2.44	2.04	0.45	0.33	0.06	0.2	0.1	0.1
M800-1	46	28.9	22.2	16.2	24.9	11.7	9.74	9.43	2.18	0.64	0.74	0.71	0.32	0.33	0.34	0.3

Membranes	Selectivity [-]											
	He/H_2				H_2/N_2				H_2/SF_6			
	0 HT	1 HT	2 HT	3 HT	0 HT	1 HT	2 HT	3 HT	0 HT	1 HT	2 HT	3 HT
M500-1	0.73	0.90	0.89	0.97	23.23	27.85	25.80	23.72	2090.91	294.18	192.26	176.54
M600-1	0.79	1.46	1.73	1.94	25.66	**85.51**	85.17	74.28	7287.62	1779.83	947.78	170.20
M700-1	1.11	0.89	2.09	4.24	27.98	25.83	20.60	9.94	1159.93	192.34	86.16	32.87
M800-1	1.86	2.45	2.28	1.72	11.43	18.52	13.23	13.20	78.61	35.87	28.70	28.89

Temperature dependence of gas permeance through microporous AHPCS membranes.

In this study, the temperature dependence of He, N_2, and H_2O permeance was examined for AHPCS membranes fired at 550, 600, and 700 °C. As shown in Fig. S6 similar to M550 in Fig. 11, M600 and M700 also showed a linear relationship between the He permeance and reciprocal temperature, suggesting an activated diffusion mechanism.[12] Significantly, H_2O showed decreased permeance with increasing temperature, which again confirmed the surface diffusion properties of H_2O.
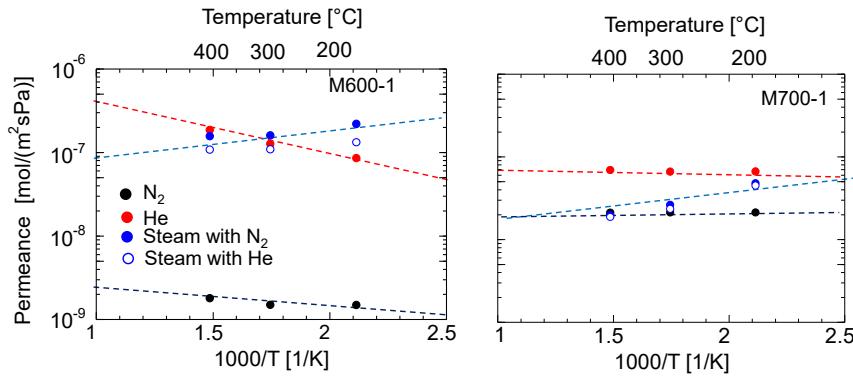
Fig. S6. Temperature dependence at various firing temperatures membranes for M600-1 (left) and M700-1 (right).

Comparison of H₂O/N₂, H₂O/H₂, and H₂O/He of AHPCS-SiC derived membranes with other membranes.

Table S3. Comparison of H_2O/N_2, H_2O/H_2, H_2O/He of AHPCS-SiC derived membranes with other membranes.

System	Material	Temperature [°C]	p_{water} [kPa]	Water permeance [10^{-8} mol/(m² Pa s)]	Permeance ratio	Reference
H_2O/N_2	PCS	50			107	[13]
H_2O/N_2	TFN_SU (0.2)	30	98	67	564	[14]
H_2O/N_2	TFN CU (0.2)	30	98	72	639	[14]
H_2O/N_2	TFN_U (0.2)	30	98	58	485	[14]
H_2O/H_2	Zeolite A	200			270	[15]
H_2O/H_2	modernit	200			0.7	[15]
H_2O/H_2	zeolite T				~10	[15]
H_2O/N_2	Nafion–IL–SiO2	250	100	71	130	[16]
H_2O/H_2	Zeolite A	180	10		200	[17]
H_2O/H_2	Zeolite A	>240	10		<20	[17]
H_2O/N_2	BTESE	150	130-140	1100	320	[18]
H_2O/N_2	BTESE	100	130-140		1200	[18]
H_2O/H_2	BTESE	200	11	428	4.5	[12]
H_2O/H_2	BTESE	80			170	[12]
H_2O/H_2	BTESE	200	11	470	4.0	[12]

H_2O/H_2	BTESE	200	11	370	3.7	[12]
H_2O/H_2	BTESE	200	57	287	16.4	[12]
H_2O/H_2	BTESE	150	10	514	13	[12]
H_2O/H_2	BTESE	150	10	277	82	[12]
H_2O/H_2	BTESE	150	11	388	23	[12]
H_2O/H_2	BTESE	150	11	546	6.8	[12]
H_2O/H_2	BTESE	150	11	439	7.1	[12]
H_2O/H_2	BTESE	150	56	525	32	[12]
H_2O/H_2	BTESE	150	56	399	59	[12]
H_2O/H_2	BTESE	150	56	307	178	[12]
H_2O/H_2	BTESE	150	104	545	84	[12]
H_2O/H_2	Al-BTESE	80			76	[19]
H_2O/N_2	Al-BTESE	150	200-360		59	[19]
H_2O/N_2	i-BTESE	200	200	500	350	[20]
H_2O/H_2	silica	300	25	1.3	0.17	[21]
H_2O/H_2	NaA zeolite	240	46	30	0.18	[22]
H_2O/H_2	LTA	200	2	9.1	268	[23]
H_2O/N_2	BTESE	200	14	347	164	[12]
H_2O/N_2	BTESE	200	14	386	72	[12]
H_2O/N_2	BTESE	200	14	311	34	[12]
H_2O/N_2	BTESE	200	65	276	545	[12]
H_2O/N_2	BTESE	150	13	244	1697	[12]
H_2O/N_2	BTESE	150	14	426	502	[12]
H_2O/N_2	BTESE	150	14	331	1203	[12]
H_2O/N_2	BTESE	150	14	455	112	[12]
H_2O/N_2	BTESE	150	14	367	56	[12]
H_2O/N_2	BTESE	150	64	464	1161	[12]
H_2O/N_2	BTESE	150	64	305	1491	[12]
H_2O/N_2	BTESE	150	65	390	1445	[12]
H_2O/N_2	BTESE	150	107	546	>6700	[12]
H_2O/N_2	BTESE	80			3300	[12]

H_2O/N_2	Al-BTESE	80			1100	[19]
H_2O/N_2	Al-BTESE	150	200-360		740	[19]
H_2O/N_2	silica	300	30	1.4	15	[21]
H_2O/N_2	FAU zeolite	200	550	3190	8.0	[24]
H_2O/N_2	FAU zeolite	200	550	3990	7.0	[24]
H_2O/He	TEFS-SiO_2	500	90		0.27	[25]
H_2O/N_2	LTA	200	2	8.9	59	[23]
H_2O/N_2	Nafion 115	150	96	6	1190	[26]
H_2O/N_2	Nafion 115	150	180	10	1765	[26]
H_2O/N_2	Nafion 115	150	304	15	1515	[26]
H_2O/N_2	Nafion 115	150	377	29	1580	[26]
H_2O/N_2	AHPCS	400	125	130	27	This work
H_2O/N_2	AHPCS	400	125	10	0.26	This work
H_2O/N_2	AHPCS	500	125	13	25	This work
H_2O/N_2	AHPCS	500	125	10	0.18	This work
H_2O/N_2	AHPCS	300	125	34	118	This work
H_2O/N_2	AHPCS	300	125	34	0.74	This work
H_2O/N_2	AHPCS	400	125	11	25.8	This work
H_2O/He	AHPCS	400	125	10	0.26	This work
H_2O/N_2	AHPCS	400	125	99	35.68	This work
H_2O/He	AHPCS	400	125	99	1.4	This work
H_2O/N_2	AHPCS	400	125		12.44	This work
H_2O/He	AHPCS	400	125	4	0.07	This work
H_2O/N_2	AHPCS	400	125	94	43.6	This work
H2O/He	AHPCS	400	125	87	1.57	This work
H_2O/N_2	AHPCS	400	125	10	16.7	This work
H2O/He	AHPCS	400	125	6	0.135	This work
H_2O/N_2	AHPCS	400	125	6	11	This work
H2O/He	AHPCS	400	125	4	0.086	This work
H_2O/N_2	AHPCS	400	125	53	102.45	This work
H2O/He	AHPCS	400	125	26	0.433	This work

H$_2$O/N$_2$	AHPCS	400	125	167	26	This work
H$_2$O/He	AHPCS	400	125	131	0.7	This work
H$_2$O/N$_2$	AHPCS	400	125	22	48.1	This work
H$_2$O/He	AHPCS	400	125	12	0.26	This work

References

1   M. Kanezashi, H. Sazaki, H. Nagasawa, T. Yoshioka and T. Tsuru, *J. Membr. Sci.*, 2015, **493**, 664–672.

2   H. Nagasawa, T. Niimi, M. Kanezashi, T. Yoshioka and T. Tsuru, *AIChE J.*, 2014, **60**, 4199 – 4210.

3   H.V. Pham, M. Kurata, and M. Steinbrueck, Thermo, 2021, 1, 151–167.

4   H.V. Pham, Y. Nagae, M Kurata, D. Bottomley, and K. Furumoto, J. Nucl. Mater. 2020, 529, 151939

5   M. Fukushima, Y. Zhou, Y. Yoshizawa, K. Hirao, J. Eur. Ceram. Soc., 2008, 28, 1043–1048.

6   M. Kanezhashi, T. Tsuru, Membr. Sci. Technol., 2011, 14,117–136.

7   M. Kanezashi, T. Sasaki, H. Tawarayama, H. Nagasawa, T. Yoshioka, K. Ito, T. Tsuru, J. Phys. Chem. C 2014, 118, 35, 20323–20331

8   D. W. Breck, Zeolite Molecular Sieves: Structure, Chemistry, and use, Wiley-Interscience: New York, N.Y. 1974

9   M.C. Duke, J.C.D. da Costa, D.D. Do, P. G. Gray, and G. Q. Lu, Adv. Funct. Mater. 2006;16, 1215–20.

10 M.C Duke, J.C.D. da Costa, G. Q (max) Lu, M. Petch, and P. Gray, J. Membr. Sci., 2004, 241, 325–33.

11 T. Tanaka, M. Kanezhashi, H. Nagasawa, T. Tsuru, Ind. Eng. Chem. Res., 2019, 58, 3867–3875.

12 N. Moriyama, H. Nagasawa, M. Kanezashi and T. Tsuru, *J. Membr. Sci.*, 2019, **589**, DOI:10.1016/j.memsci.2019.117254.

13 M. Kubo, K. Okibayashi, M. Kojima, R. Mano, Y. Daiko, S. Honda, S. Bernard and Y. Iwamoto, *Sep. Purif. Technol.*, 2021, **258**, DOI:10.1016/j.seppur.2020.117998.

14 H. J. Lee, Y. M. Shirke, J. Kim, H. J. Yu, C. H. Yoo, S. Back, J. D. Jeon and J. S. Lee, *J. Membr. Sci*, 2023, **665** , DOI:10.1016/j.memsci.2022.121096.

15 R. Raso, M. Tovar, J. Lasobras, J. Herguido, I. Kumakiri, S. Araki and M. Menéndez, *Catal. Today*, 2021, **364**, 270–275.

16 P. G. Ingole, M. I. Baig, W. Choi, X. An, W. K. Choi, J. D. Jeon and H. K. Lee, *Chem. Eng. Res. Des.*, 2017, **127**, 45–51.

17 J. Gorbe, J. Lasobras, E. Francés, J. Herguido, M. Menéndez, I. Kumakiri and H. Kita, *Sep. Purif. Technol.*, 2018, **200**, 164–168.

18 N. Moriyama, H. Nagasawa, M. Kanezashi and T. Tsuru, *Sep. Purif. Technol.*, 2021, **275**, DOI:10.1016/j.seppur.2021.119191.

19 N. Moriyama, M. Ike, H. Nagasawa, M. Kanezashi and T. Tsuru, *RSC Adv.*, 2022, **12**, 5834–5846.

20 N. Moriyama, H. Nagasawa, M. Kanezashi and T. Tsuru, *J. Membr. Sci*, 2021, **620**, DOI:10.1016/j.memsci.2020.118895.

21 T. Tsuru, *J. Jpn. Pet. Inst.*, 2011, **54**, 277–286.

22 S. M. Lee, N. Xu, J. R. Grace, A. Li, C. J. Lim, S. S. Kim, F. Fotovat, A. Schaadt and R. J. White, *J. Eur. Ceram. Soc.*, 2018, **38**, 211–219.

23 K. Aoki, K. Kusakabe and S. Morooka, *Ind. Eng. Chem. Res.*, 2000, **39**, 2245–2251.

24 T. F. Mastropietro, A. Brunetti, P. F. Zito, T. Poerio, H. Richter, M. Weyd, S. Wöhner, E. Drioli and G. Barbieri, *Sep. Purif. Technol.*, 2015, **156**, 321-327.

25 M. Kanezashi, N. Hataoka, R. Ikram, H. Nagasawa and T. Tsuru, *AIChE J.*, 2021, **67**, DOI:10.1002/aic.17292.

26 H. Azher, C. A. Scholes, G. W. Stevens and S. E. Kentish, *J. Membr. Sci*, 2014, **459**, 104–113.